J Nanopart Res (2022) 24:271
https://doi.org/10.1007/s11051-022-05645-7

RESEARCH PAPER

Exploration of the potential of Co/Cu co-doped Fe_2O_4 for medical applications: nanostructure, catalytic properties, and blood compatibility

Bestenur Yalcin

Received: 11 May 2022 / Accepted: 5 December 2022 / Published online: 16 December 2022

Abstract Nano-sized metal oxides with magnetic properties are a group of scientifically valuable materials whose application areas are increasingly diverse. This study investigates the structural, morphological, magnetic, photocatalytic, and hemolytic properties of $CoCuFe_2O_4$ nanoparticles (NPs) synthesized by co-precipitation method. Photocatalytic and biological properties of the samples were investigated by following crystal violet (CV) photocatalytic degradation reactions and hemolysis experiments, respectively. X-ray diffraction analysis (XRD) and scanning electron microscope (SEM) were used to analyze crystalline properties and morphological structure of nano-sized ferrites. Photocatalysis tests showed that $CoCuFe_2O_4$ NPs degraded 64.9% of the total organic dye after 420-min exposure to 254 nm irradiation. Coercivity (H_c) and saturation magnetization (M_s) of $CoCuFe_2O_4$ NPs were determined as 1000 Oe and 15.44 emu/g, respectively. Hemolysis tests showed an average hemolysis ratio (AHR) of 12.4% for human erythrocytes subjected to 5.0 mg mL^{-1} $CoCuFe_2O_4$ concentration, while it was only 2.2% for those of exposed to 1.0 mg mL^{-1} $CoCuFe_2O_4$. In addition, at both $CoCuFe_2O_4$ concentrations, spectrophotometric evidence was found indicating hemoglobin oxidation under the effect of reactive oxygen species (ROS) formed on the nanoparticle surface.

Keywords Co-precipitation method · Fe_2O_4 · Hemolysis · Magnetic properties · Photodegradation

B. Yalcin (✉)
Vocational School of Health Services, Department of Medical Laboratory Techniques, Bahcesehir University, 34353 Istanbul, Turkey
e-mail: bestenur.yalcin@eng.bau.edu.tr

Introduction

Nano-metal oxides (NMOs) have received enormous attention due to their structural stability and high magnetic properties [1, 2] and regarded as valuable materials in medicinal area such as magnetic resonance imaging and magnetic hyperthermia [3, 4]. They have a talent to form biological interactions at the cellular level, enabling targeted drug delivery applications and node detections in tumors [5, 6]. They also have well-characterized catalytic performances towards the selective oxidation of carbon monoxide, decomposition of hydrogen peroxide, and degradation of synthetic colorants and have been extensively studied for both medicinal and environmental applications [7, 8].

Among NMOs, iron-containing derivatives having spinel configuration have magneto-crystalline anisotropy, high mechanical and chemical stability, and well-characterized magnetic properties [9–11]. Spinel ferrites have a general molecular formula of MFe_2O_4 and constituted by cubic structured unit cells. M represents a divalent metal cation such as Mn^{2+}, Ba^{2+}, Ni^{2+}, Fe^{2+}, Cu^{2+}, Zn^{2+}, or Co^{2+}. Face-centered cubic

lattice structure of spinel ferrites allows the formation of tetrahedral and octahedral coordination sites occupied by M^{2+} and/or Fe^{3+} ions. It is also possible to produce double ferrites having a general formula of $M'_{1-x}M''_xFe_2O_4$ by the isomorphic substitution of M. Spinel ferrites are very popular in scientific and technological area due to their adjustable physical, chemical, and physicochemical properties under the effect of external magnetic field and potential medical applications [12, 13]. Ferrites can exhibit high saturation magnetization depending on the particle size and morphological structure [14]. This feature allows to obtain ferrite-based materials that can respond quickly and efficiently to variable magnetic field applications. When evaluated in terms of photodegradation applications, the presence of a second metal doped into the ferrite structure allows to obtain photocatalysts with narrower band gaps, and therefore, highly efficient reactions can be proceeded even under ultraviolet/visible light [15]. Among spinel ferrites, especially cobalt ferrite ($CoFe_2O_4$) and copper ferrite ($CuFe_2O_4$) are of great interest in physical, chemical, and medical aspects due to the ability to control of their physicochemical properties as well as perfect mechanical properties and chemical stability [16, 17].

The mechanical properties and chemical stability of double ferrites and their superparamagnetic behavior that can vary depending on particle size [9] make these nano-sized materials tough competitors against traditional iron oxide structures such as magnetite (Fe_3O_4) and hematite (Fe_2O_3). Besides the ability of Fe_3O_4 and Fe_2O_3 to form reactive oxygen species, the biocompatibility of these species can also be improved by double ferrites obtained by isomorphic replacement of a second element atom with Fe.

Having inferior toxicity, high bio/cell compatibility, and showing high structural stability in physiological conditions are the main characteristics of materials planned to be used for biological and medicinal purposes. For example, superparamagnetic $CoFe_2O_4$ NPs proven as biocompatible were used in a controlled drug delivery system triggered by the application of an alternating magnetic field [18]. It was emphasized in another study that $CoFe_2O_4$ NPs display biocompatibility against both erythrocytes and breast cancer cells even without the presence of an exterior immune-specific coating [19]. Moreover, negligible hemolysis ratios offer significant biocompatibility which is essential for in vivo biomedical applications such as intravenous drug delivery, magnetic hyperthermia, and node tracer injections [20, 21].

Although being a heavy metal, Cu has a vital role in biological processes. In trace amounts, Cu is being required as co-factor of numerous enzymes involved in biological redox reactions [22]. Co is also vital as taking part in cyanocobalamin ($C_{63}H_{88}CoN_{14}O_{14}P$) and methylcobalamin ($C_{63}H_{91}CoN_{13}O_{14}P$) which are the most stable and biologically active forms of vitamin B12 [23]. On the other hand, elevated concentrations of both Co and Cu show toxic effects in biological systems. ROS produced by Co and Cu containing NPs may cause high levels of oxidative stress on tissues leading to failure of cell functions, inflammatory reactions, and cardiovascular diseases as well as cancer. However, some literature studies highlight the potential of nanostructures containing Co and Cu, especially in medical and biomedical applications. For example, in the study of Sattarahmady et al., dextrin-coated Co-Zn nano-ferrites ($Zn_{0.5}Co_{0.5}Fe_2O_4$) synthesized by co-precipitation technique were declared as having potential in MRI [24]. Properties of porphyrins attached on cobalt oxide surfaces were also investigated in terms of metalation which is one of the important interactions between porphyrins and metal oxide surfaces, due to the effect of metal ion incorporated in the porphyrin ring on chemical, electrical, and optical characteristics [25]. In another study, the applicability of cobalt protoporphyrin-loaded silica NPs in photoacoustic imaging by subcutaneous and myocardial injection approaches was proposed [26]. Another study reports the synthesis of ultrasmall CuO (Us-CuO) NPs showing enzyme-mimicking properties and broad-spectrum ROS scavenging ability. Also, researchers emphasize the cell-protective effects of Us-CuO NPs and their potential use in the treatment of ROS-related diseases [27].

Materials designed for medical purposes must be well-characterized in terms of their biocompatibility. Hemolysis tests are one of the well-accepted scientific ways to establish the biocompatibility of a synthetic material [28, 29]. Magnetic NPs, especially ferrites, are being studied for their usability in biomedical applications such as controlled drug release, hyperthermia applications, selective protein adsorption, and magnetic resonance imaging (MRI) [30–33]. Biological incompatibility between blood

components (including RBCs) and iron-containing molecules arises from the oxidizing properties of hypervalent iron towards organic molecules [34]. A study conducted by Xiong et al. emphasized the enhanced reduction ability of Fe/Cu bimetallic particles and broadened reduction efficiency in the pH range of 3.0–9.0 in respect to pure Fe [35]. Reactivity of Fe^{3+} in biological systems can be adjusted by the incorporation of ferrite structures. Undesirable interactions between synthetic materials and blood components caused by the presence of Co and Cu ions in the structure of synthetic materials can be reduced or prevented by using ferrites. Ferrite structures show higher biocompatibility compared to conventional iron oxides. The synthesis of ferrites at nanoscale provides high photocatalytic, electrical, and magnetic properties in addition to biocompatibility. Thus, in this study, $CoCuFe_2O_4$ NPs were synthesized and investigated in terms of their material properties as well as biological potential. The aim of this study is to provide data about the advantages that $CoCuFe_2O_4$ NPs can provide in medical and biomedical fields.

Especially in the last few decades, design of new materials especially in the nanometer scale has become a very popular research area. Designing new materials with unique and/or improved properties for various application areas such as electronics, sensors, medicine, and biotechnology makes this area of research much more valuable. Up to date, many studies have been conducted on nano-sized metal oxides which were focused mainly on the material properties rather than the potential for use in medical area. Literature research shows that MFe_2O_4 and $M'_{1-x}M''_xFe_2O_4$ nanomaterials have a high potential especially in terms of biomedical applications [36–38]. However, there are only limited number of studies presented to the literature regarding the properties of $CoCuFe_2O_4$, and these studies have focused mainly on the synthesis conditions and catalytic properties of these NPs [39, 40]. Very few studies have been conducted on the biological properties of $CoCuFe_2O_4$ NPs. Thus, in order to prove the accuracy of the predictions on the potential of $CoCuFe_2O_4$ NPs, the interactions between the ferrite structures synthesized in this study and blood components were investigated by hemolysis tests. This study also reports the synthesis and material properties of $CoCuFe_2O_4$ NPs as well as the photocatalytic properties of $CoCuFe_2O_4$ NPs which have not been reported adequately.

Experimental part

Nanoparticle synthesis

Synthesis procedure of $CoCuFe_2O_4$ nano-ferrites by co-precipitation method was summarized in Fig. 1. Iron(III) nitrate nonahydrate ($Fe(NO_3)_3.9H_2O, \geq 99.95\%$, Sigma Aldrich), cobalt(II) nitrate hexahydrate ($Co(NO_3)_2.6H_2O, \geq 99.0\%$, Sigma Aldrich), and copper nitrate trihydrate ($Cu(NO_3)_2.3H_2O, \geq 99.0\%$, Sigma Aldrich) were used in the synthesis. In a typical experimental procedure to synthesize $CoCuFe_2O_4$ nano-ferrites, a 100-mL aqueous solution of $Fe(NO_3)_3.9H_2O$, $Co(NO_3)_2.6H_2O$, and $Cu(NO_3)_2.3H_2O$ was prepared with 0.2 M, 0.05 M, and 0.05 M concentrations, respectively. All reagents used in the nanoparticle synthesis were of analytical grade (Alfa Aesar). In nanoparticle syntheses, 30 µL of oleic acid was added to the reaction medium as the surfactant to prevent aggregation of NPs. Reaction mixture was continuously sonicated using an ultrasonic bath (Bandelin RK103H) for 2 h at 80 °C. Next, the pH of the reaction mixture was adjusted to pH 9 with NaOH added dropwise to form fine particles of solid hydroxides of metals (Eq. 1). Simultaneously, the mixture was maintained in ultrasonic bath for an additional 1 h to allow the transformation of metal hydroxides to metal oxides (Eq. 2). Next, distilled water was added to the precipitate and centrifuged (NUVE NF400) at 5000 rpm for 10 min. This purification process was repeated five times to remove the unreacted hydrates, unwanted impurities, and excess surfactant from the obtained product. $CoCuFe_2O_4$ NPs were than dried at 80 °C under vacuum for 8 h. $CoCuFe_2O_4$ NPs were calcined at 500 °C for 2 h at atmospheric conditions. As confirmed by XRD analysis, the final product obtained was NPs of cobalt–copper ferrite ($CoCuFe_2O_4$) with spinel structure:

$$Cu^{2+}(aq) + Co^{2+}(aq) + 2Fe^{3+}(aq) + OH^{-}(aq) \rightarrow Cu(OH)_2.Co(OH)_2.2Fe(OH)_3(s) \quad (1)$$

$$Cu(OH)_2.Co(OH)_2.2Fe(OH)_3(s) \rightarrow CoCuFe_2O_4.nH_2O(s) \quad (2)$$

Structural analysis

The crystal properties of the $CoCuFe_2O_4$ NPs were characterized by XRD measurements using fully computerized X-ray diffractometer (PANalytical

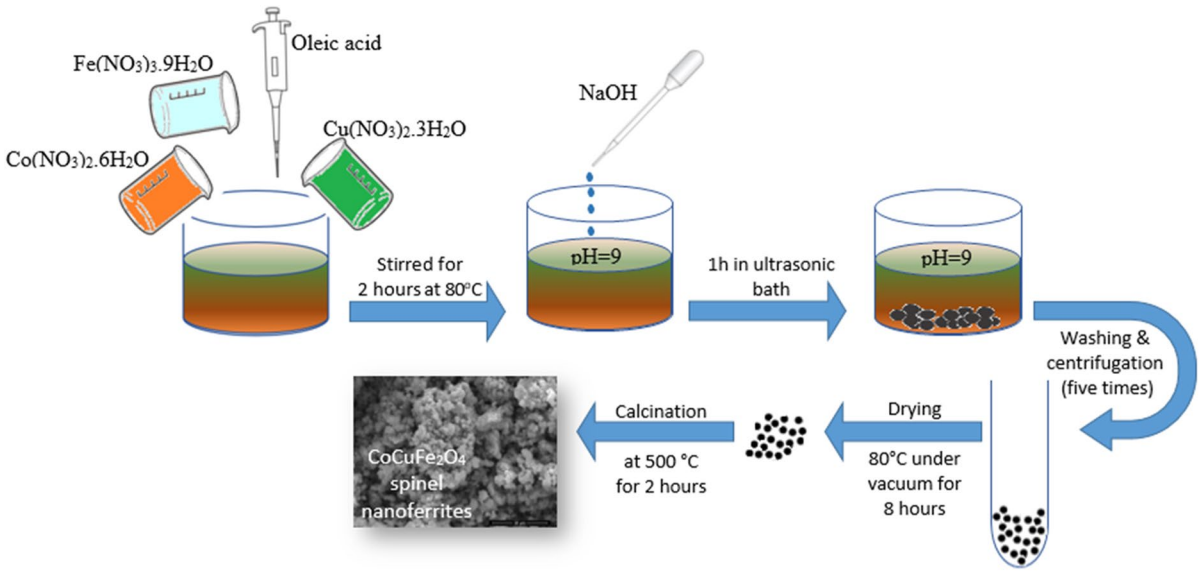

Fig. 1 Schematic illustration of the synthesis of $CoCuFe_2O_4$ nano-ferrites by co-precipitation method

X'pert Powder 3) with CuKα (λ = 1.5418 Å) radiation. Characterizations were performed at room temperature and patterns were recorded with a scanning speed of 3 (°)/min in the range of 2θ = 10° − 90° and a step size of 0.02°. The morphological characteristics of the $CoCuFe_2O_4$ NPs were investigated by using SEM (Zeiss EVO MA). Before SEM analysis, $CoCuFe_2O_4$ NPs were coated with gold–palladium under argon atmosphere to make the surface electrically conductive. Shape, surface morphology, length, and diameter of NPs were examined by SEM micrographs with different magnifications. Optical properties of the $CoCuFe_2O_4$ NPs were characterized by using a UV-Spectrometer (Shimadzu 2600) between 300 and 1000 nm. Magnetic characteristics were investigated through a vibrating sample magnetometer (Lake Shore 7304), operating in the temperature range of 15 K to 300 K.

Photocatalytic performance of $CoCuFe_2O_4$ NPs

Photocatalytic degradation experiments of crystal violet (CV) in the presence of $CoCuFe_2O_4$ NPs were evaluated using an aqueous dispersion of NPs (1.0 mg mL^{-1}) depending on the varying photodegradation time. CV solution with a concentration of 2.5×10^{-6} M was used in photocatalysis tests. In order to ensure that the CV reaches the equilibrium adsorption/desorption condition on the nanoparticle surfaces, magnetic stirring was applied continuously in the dark for 1 h before photocatalysis. Thereafter, aqueous dispersions of NPs in CV solution were exposed to 254 nm irradiation in cylindrical open top Pyrex reactors. The irradiation was carried out using a couple of UV lamps (45 W each) which was placed vertically on the reaction vessels at a distance of 40 cm. During the photodegradation process, 1.5 ml samples of CV dispersions were withdrawn at appropriate time intervals and subsequently centrifuged at 4000 rpm for 3 min to settle the NPs down. Supernatants were analyzed for undegraded CV content using Shimadzu UV mini 1240 UV–Vis spectrophotometer at $\lambda_{max} = 591$ nm. Distilled water was used as a reference.

Blood compatibility tests

Susceptibility of erythrocytes (red blood cells, RBCs) to hemolysis in the presence of $CoCuFe_2O_4$ NPs was investigated. Venous blood samples were drawn from healthy adult volunteers (35–38 age female) and anticoagulated with the aqueous solution of 3.2% trisodium citrate. Blood:trisodium citrate ratio was 9:1. Blood:anticoagulant mixture was diluted with phosphate buffer solution (pH 7.35) and centrifuged at 5000 rpm for 3 min to precipitate the red blood cells (RBCs). After discharging the supernatant, RBCs were diluted with PBS. Solutions

of RBC's were prepared freshly and kept at room temperature during the tests. 1.0 ml of RBC stock solution was added to 5.0 ml of $CoCuFe_2O_4$ nanoparticle suspensions prepared at concentrations of 1.0 mg mL^{-1} and 5.0 mg mL^{-1}. The prepared samples were incubated at 37 °C, which is the physiological temperature, for 3 h. NP erythrocyte suspensions were kept in the dark during the incubation period in order to avoid the effect of ROS that can be formed by the nanoparticles under the influence of ambient light. Each test was repeated twice, and the hemolysis percentages were averaged. After the incubation period, dispersions were centrifuged at 4000 rpm for 5 min, and absorbance of the supernatant was measured between 400 and 700 nm using a UV–Vis spectrophotometer. Absorption spectra were interpreted to detect the possible presence of hemoglobin (Hb) released into the environment following the lysis of RBCs.

The hemolysis ratio of each sample was calculated using the absorbance values at 540 nm corresponding to the absorption maxima of oxyhemoglobin (OxHb) in accordance with the following equation [41]:

$$\%Hemolysis = \frac{A_T - A_{NC}}{A_{PC} - A_{NC}} \times 100 \quad (3)$$

Test results of RBCs in PBS alone were used as negative control (*NC*), whereas the results of RBCs in pure water was used as positive control (*PC*). A_T refers for the absorbance value of test sample at 540 nm. Erythrocyte-$CoCuFe_2O_4$ interactions, $CoCuFe_2O_4$-induced erythrocyte deformations, and overall erythrocyte morphology before and after incubation with $CoCuFe_2O_4$ NPs were examined using a Nikon Eclipse E100 optical microscope.

Results and discussions

In this study, $CoCuFe_2O_4$ NPs were synthesized by co-precipitation which is a convenient method for the synthesis of NMOs. In this method, simple precursor solutions are used to synthesize NMOs with desired properties. Moreover, the co-precipitation method allows a rapid, simple, low-cost synthesis route to easily control the properties of the final product. In the following section, the structural, morphological, magnetic, photocatalytic, and biological properties of $CoFe_2O_4$ NPs synthesized by the co-precipitation method in this study are reported.

XRD analysis

Characteristic powder XRD pattern confirmed the crystal structure of $CoCuFe_2O_4$ NPs (Fig. 2). Moreover, the formation of cubic structured spinel lattice was approved by all diffraction peaks for the $CoCuFe_2O_4$. No additional reflections were detected for the secondary phases in the XRD diffraction patterns corresponding to the oxides. In addition, it was determined that $CoCuFe_2O_4$ NPs belong to the Fd-3 m space group (PDF Card No.: 98–019-1044). The lattice parameter, a, was calculated using Eq. 4:

$$a_{exp} = d_{hkl}(h^2 + k^2 + l^2)^{1}/_{2} \quad (4)$$

The crystallite size (D) of the $CoCuFe_2O_4$ NPs was calculated by Debye–Scherrer expression (Eq. 5) considering the full width at half maximum (FWHM) of the most intense peak (113):

$$D = 0.9\lambda/\beta cos\theta_B \quad (5)$$

In Eq. 5, λ, β, and θ_B are the X-ray wavelength of CuKα, the FWHM of the diffraction peak (113), and the Bragg diffraction angle, respectively. The calculated values of D and a, for $CoCuFe_2O_4$ NPs, were given in Table 1.

SEM analysis

The surface morphology of $CoCuFe_2O_4$ NPs synthesized by the co-precipitation method was investigated using scanning electron microscopy–energy dispersive spectroscopy (SEM–EDS) at an accelerating voltage of 30 kV. SEM images showed that $CoCuFe_2O_4$ NPs were not monodispersed in terms of size and shape and highly agglomerated (Fig. 3). SEM images showed that $CoCuFe_2O_4$ NPs were agglomerated as reported in previous studies [42, 43].

The chemical composition of $CoCuFe_2O_4$ NPs was given by the EDS spectrum reported in Fig. 4. The information obtained from the EDS spectrum was used in the identification of the presence of Co, Cu, and Fe in ferrite structure as well as for the

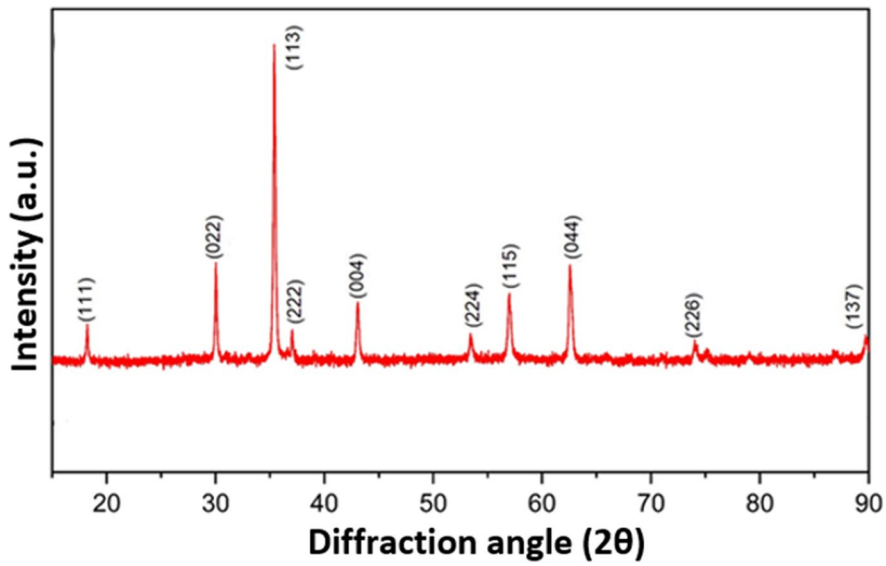

Fig. 2 X-ray diffraction patterns of $CoCuFe_2O_4$ nanoparticles

Table 1 Calculated values of the crystallite size (D) and lattice parameter (*a*) of $CoCuFe_2O_4$ nanoparticles

Sample	Crystallite size D (nm)	Lattice parameter *a* (Å)
$CoCuFe_2O_4$	40.537	8.41

confirmation of the successful result of Co and Cu co-doping into the Fe_2O_4 structure (Fig. 4).

Band gap calculation

The reflectance spectra of the $CoCuFe_2O_4$ NPs were obtained by UV–Vis diffuse reflectance measurements in 300–1000 nm wavelength range. Figure 5 inset graph shows the absorption edge which is close to 378 nm. The reflectance $F(R)$ is proportional to the absorption coefficient (α). It was calculated by using the Kubelka–Munk function [44]:

$$F(R) = \frac{(1-R)^2}{2R} \tag{6}$$

The optical band gap E_g for the photon energy ($h\upsilon$) and the absorption coefficient (α) was calculated by using the following equation:

$$\alpha h\upsilon = \mathrm{k}(\mathrm{h}\upsilon - E_g)^{1/n} \tag{7}$$

In Eq. (7), k and E_g are the energy-independent constant and the optical band gap, respectively. $F(R_\alpha)$ is proportional to α and, n was taken 1/2 and 2 for direct and indirect band gaps, respectively. Since n is taken to be 1/2 for directly allowed transitions, Eq. (7) becomes

$$F(R_\alpha)h\upsilon = \mathrm{k}(\mathrm{h}\upsilon - E_g)^2 \tag{8}$$

In other words, $(F(R_\alpha)h\upsilon)^2 = k^2(\mathrm{h}\upsilon - E_g)$. The slope of the graphs of $(F(R_\alpha)h\upsilon)^2$ was approximated by using a linear fit.

The direct band gap energy E_g was calculated by the linear approximation of the slope of the graph of $(F(R_\alpha)\ h\upsilon)^2$ to the photon energy where $F(R_\alpha) = 0$, namely, $E_g = h\upsilon$. The extrapolation of linear fit onto photon energy axis gives the E_g value. Direct and indirect band gap energies of CoCu-ferrite NPs were found as 1.93 eV and 0.6 eV, respectively. Band gap energy depends on carrier concentration, crystallite size, lattice strain, grain size, and the size effect of the dopant metal atoms in CoCu-ferrite lattice. In the study of Chavan and Naik [45], $Ni_{1-x}Mg_xFe_2O_4$ ($x = 0.0$, 0.1, 0.2, 0.3, 0.4, and 0.5) NPs were synthesized by auto-combustion method, and band gap values of samples were found between 2.84 and 2.94 eV. In another study conducted by Khan et al. [46], the band gap value of bismuth ferrite ($BiFeO_3$) NPs was calculated as 2.84 eV. Siva et al. [47] studied

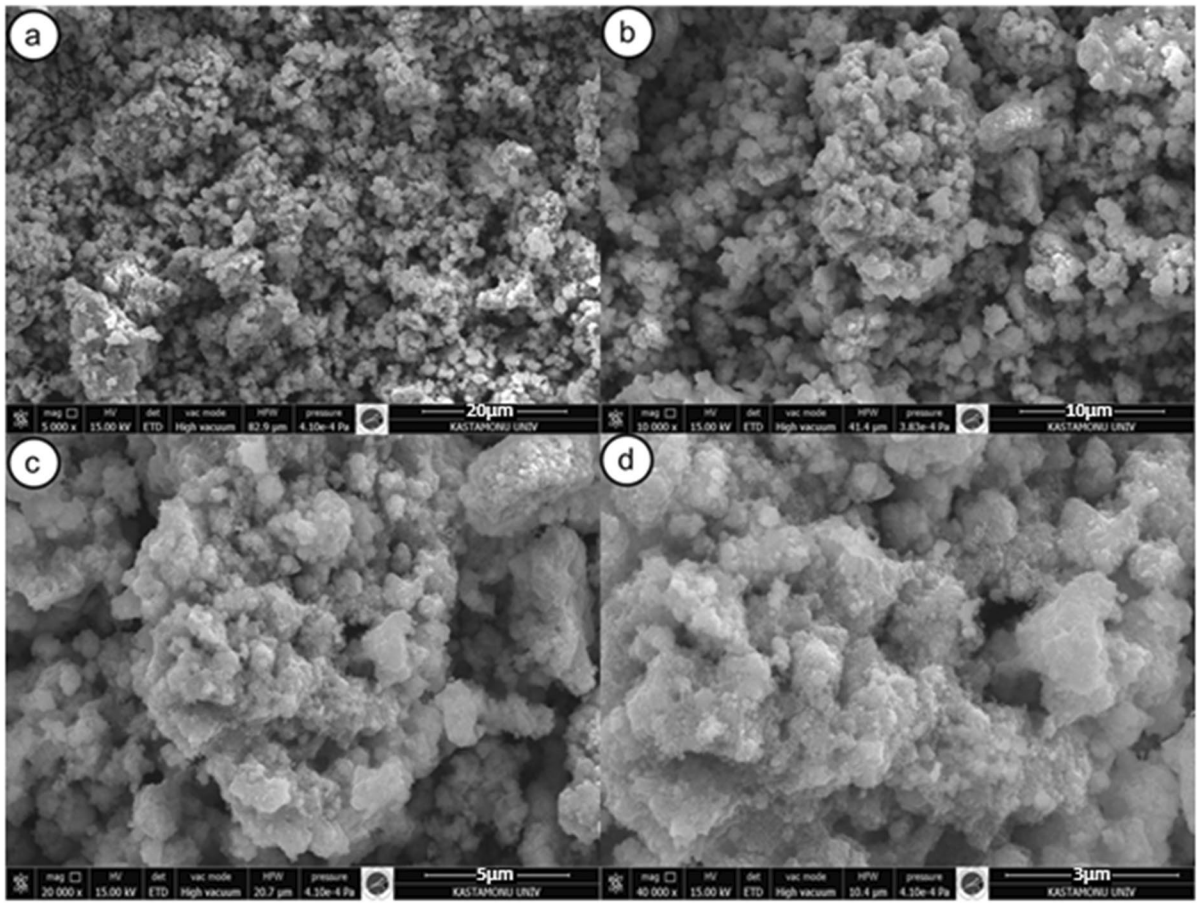

Fig. 3 SEM images of $CoCuFe_2O_4$ nanoparticles for 5 KX, 10 KX, 20 KX, and 40 KX magnifications in **a**, **b**, **c**, and **d**, respectively

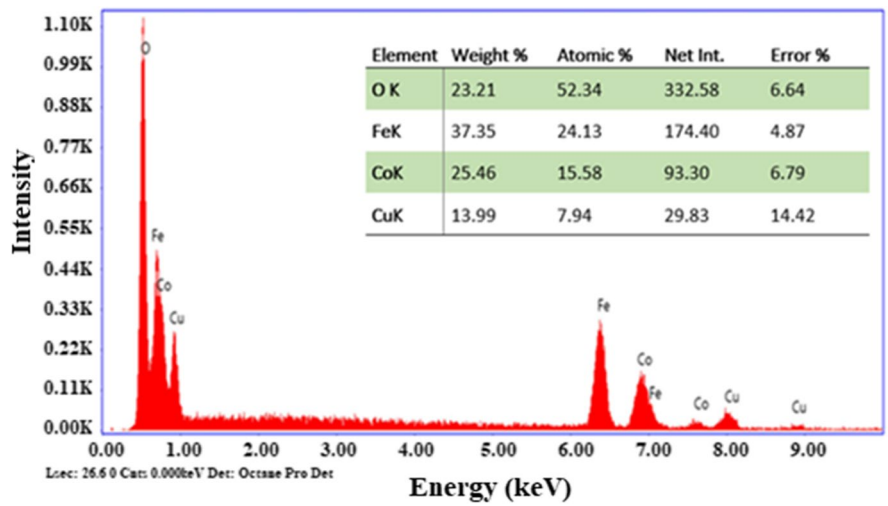

Fig. 4 EDS spectrum of $CoCuFe_2O_4$ nanoparticles

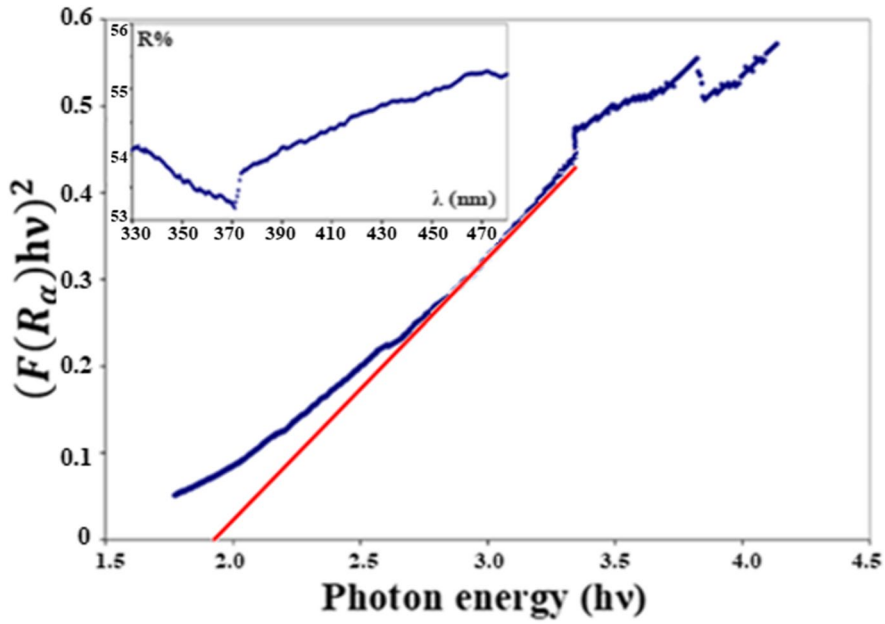

Fig. 5 The plot of $(F(R_\alpha)h\nu)^2$ as a function of photon energy (hν) and the linear fit for the $CoCuFe_2O_4$ nanoparticles. Inset: the dependence of *R* in the range of 300 nm < λ ≤ 480 nm

the material properties of $CoCuFe_2O_4$ NPs synthesized by hydrothermal method. In that study where the optical band gap was determined by Tauc equation, direct and indirect band gap values were calculated as 2.74 eV and 1.83 eV for $CoCuFe_2O_4$ NPs. Hammad et al. [48] explored the decreasing trend in band gap values of $Cu_{1-x}Co_xFe_2O_4$ ($x = 0.2$, 0.4, 0.6, 0.8, and 1.0) NPs (from 3.65 to 3.20 eV) with increasing content of Co^{2+}. Thus, in the current study, the calculated band gap values for $CoCuFe_2O_4$ NPs were found to have improved compared to literature studies.

Magnetic behavior

The magnetic nature of the $CoCuFe_2O_4$ NPs was characterized by using a vibrating magnetometer. Magnetic measurements were conducted in the range of ± 1 T at room temperature. From the obtained data, the graph of magnetization dependent on magnetic field is shown in Fig. 6. The magnetic properties (coercivity (H_c) and saturation magnetization (M_s)) of $CoCuFe_2O_4$ spinel ferrites can be seen in Table 2 and Fig. 6. Moreover, it can be seen in Fig. 6 that the magnetization curve exhibits a narrow hysteresis.

The field dependence of the magnetization (M) close to the saturation value was calculated by using the formula below [49]:

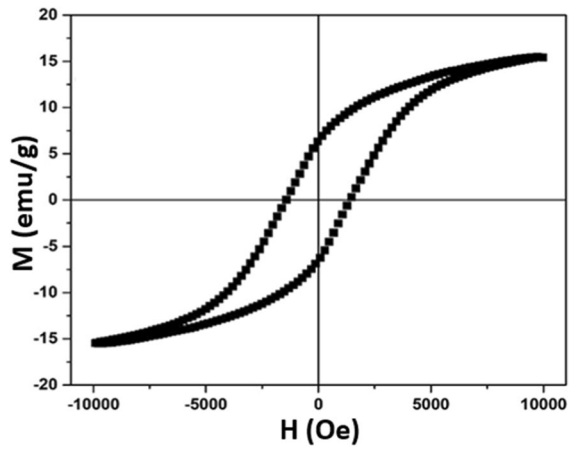

Fig. 6 M versus H plots measured for $CoCuFe_2O_4$ nanoparticles at room temperature

Table 2 Coercivity field, magnetic saturation, and parameter related to the magneto-crystalline anisotropy values of $CoCuFe_2O_4$ nanoparticles at room temperature

Sample	H_c (Oe)	M_s (emu/g)	β
$CoCuFe_2O_4$	1000	15.44	−0.443

$$M = M_s[1 - \frac{\beta}{H^2}] \quad (9)$$

where H is the applied magnetic field, β is a parameter related to the magneto-crystalline anisotropy, and Ms is the saturation magnetization. Calculated values (M_s, H_c, and β) for the $CoCuF_2O_4$ NPs are depicted in Table 2.

The plots of magnetization as a function of $1/H^2$ and linear fit for the $CoCuFe_2O_4$ NPs was depicted in Fig. 7. β and M_s values was found by the linear fitting of the slope of the graph as shown in Fig. 7 and tabulated in Table 2. In this study, M_s, H_c, and β values obtained for $CoCuFe_2O_4$ NPs were found to be compatible with the studies in the literature [44, 49].

Photocatalytic properties

Although oxidative stress has adverse effects on various biological systems, ROS produced by metal oxide particles can also be used to remove various pollutants such as paint, antibiotics, and biological wastes from the environment by photocatalytic degradation.

The photocatalytic properties of $CoCuFe_2O_4$ NPs were investigated by UV − Vis spectroscopy in the wavelength range of 400–700 nm. Absorbance values at 591 nm corresponding to the absorption maxima of CV were recorded at special time intervals and used to calculate the concentration of undegraded (remaining) CV in the solution. Time-dependent variation of the UV–Vis spectra lines of the non-photodegraded CV in an aqueous suspension of $CoCuFe_2O_4$ NPs shows the decrease of the characteristic band intensity at 591 nm over the range of 0–7 h (Fig. 8). This change under the effect of 254 nm irradiation indicates that the CV has been successfully photodegraded by $CoCuFe_2O_4$ NPs.

The decolorization percentages of CV solutions were calculated using the equation given as follows [50]:

$$Percentage\ of\ decolorization = [\frac{C_o - C_t}{C_o}] \times 100 \quad (10)$$

where C_o and C_t define for the initial CV concentration and the concentration of CV at time t, respectively.

It was observed that $CoCuFe_2O_4$ NPs were able to degrade 64.9% of total CV at the end of 420 min. The mechanism for the degradation of CV in the presence of $CoCuFe_2O_4$ NPs follows the below mentioned route. Irradiation of $CoCuFe_2O_4$ NPs causes excitation and shift of electrons from valence band (VB) to the conduction band (CB) and electron–hole pairs ($e^- - h^+$) form (Eq. 11). Holes (h^+) react with water molecules and form HO^*, while electrons in conduction band (e^-) combines with O_2 to produce O_2^{-*} (Eq. 12–14). Formation of other reactive intermediates such as hydroperoxyl radical (HO_2^*) and

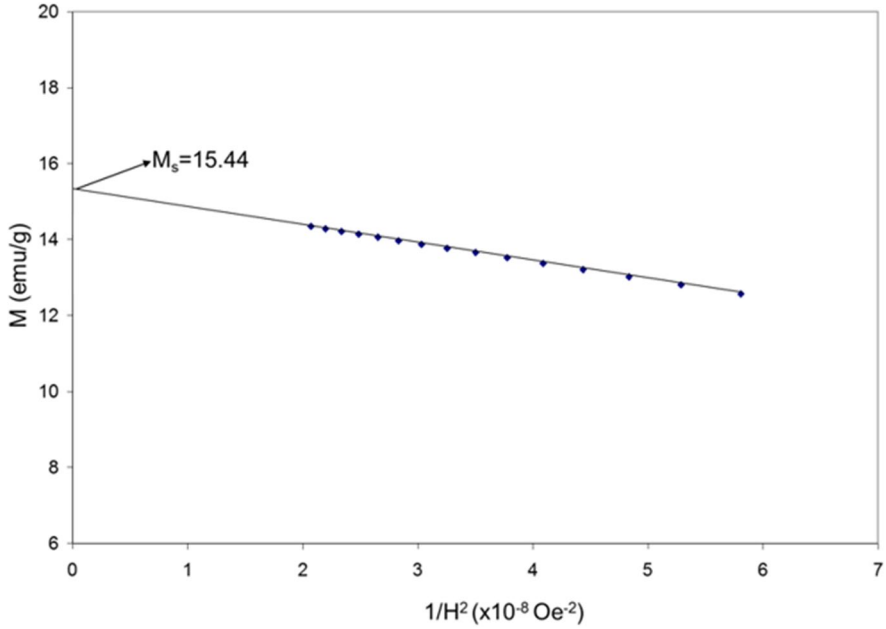

Fig. 7 Plots of M_s versus $1/H^2$ obtained in $CoCuFe_2O_4$ samples at T = 300 K

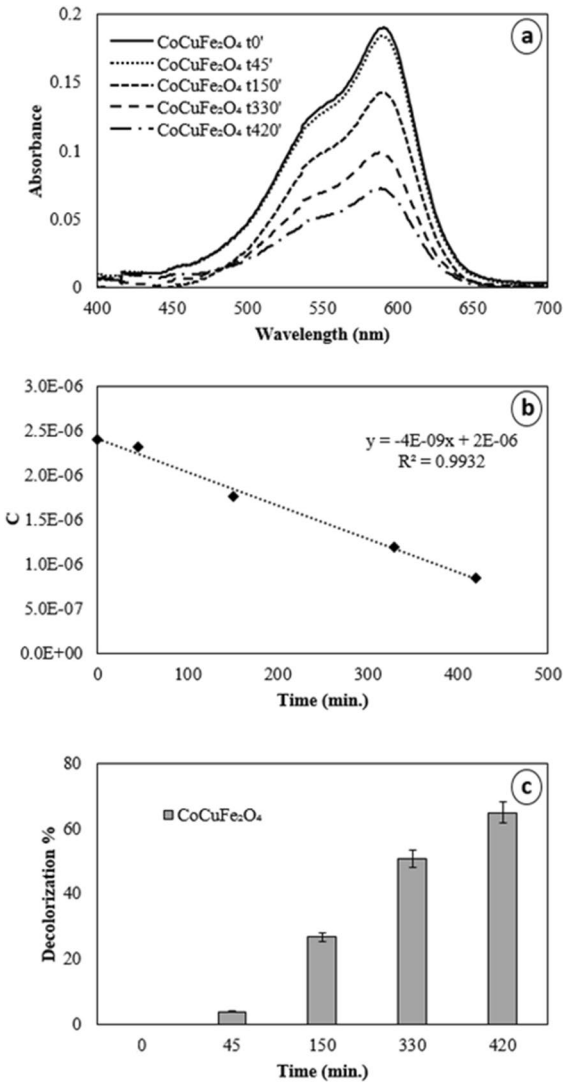

Fig. 8 **a** UV–Vis spectra of CV as a function of time in the presence of $CoCuFe_2O_4$ under 254-nm irradiation, **b** plot for the zero-order degradation kinetics, and **c** degradation percentages varying with time

H_2O_2 is then followed (Eq. 15–16) [51]. HO^*, HO_2^*, and O_2^{-*} radicals are strong oxidizing agents towards CV and other organic molecules and lead to their degradation into non-toxic molecules such as CO_2 and H_2O (Eq. 17). Schematic illustration of the photocatalytic effect of $CoCuFe_2O_4$ and photodegradation mechanism of CV were given in Fig. 9:

$$CoCuFe_2O_4 + h\nu \rightarrow CoCuFe_2O_4(e^-) + CuFe_2O_4(h^+) \quad (11)$$

$$e^- + O_2 \rightarrow O_2^{-*} \quad (12)$$

$$h^+ + H_2O \rightarrow H^+ + HO^- \quad (13)$$

$$h^+ + HO^- \rightarrow HO^* \quad (14)$$

$$O_2^{-*} + H^+ \rightarrow HO_2^* \rightarrow\rightarrow H_2O_2 + O_2 \quad (15)$$

$$H_2O_2 + O_2^{-*} \rightarrow HO^* + HO^- + O_2 \quad (16)$$

$$O_2^{-*}, HO^* + CV \rightarrow \text{Degradation products of CV} \quad (17)$$

To investigate the kinetics of photodegradation reactions, three different kinetic models were applied; those were zero order, first order, and second order [52–54]. Equations describing these kinetic models, rate constants (k, k_1, and k_2) and correlation coefficients (R^2) were listed in Table 3. In each equation, C and Co represent the concentration of CV after a certain irradiation time (t) and initial concentration of CV at $t = 0$, respectively.

Among the three kinetic models tested, the kinetic expression that most successfully described the photodegradation reaction of CV by $CoCuFe_2O_4$ NPs was the zero-order kinetic model having the highest correlation coefficient (R^2) 0.9932. $CoCuFe_2O_4$ NPs exhibited UV-irradiated photocatalytic activity which strongly depend on the formation of HO^* radicals which are generated through the transition of photo-excited electrons from valence band to conduction band.

Blood compatibility tests

NPs can affect physical appearance and chemical parameters of various cells including the erythrocytes. Alterations in the morphology of erythrocytes change the elastic properties of cells and damage the rheological properties and respiratory functions [55, 56]. Cellular response in the presence of a synthetic material is an important subject of interest. Since the erythrocyte membrane is based on a similar principle of molecular organization with the cell membranes of other tissues which make up the biological system, possible responses of other membrane systems can be predicted by examining

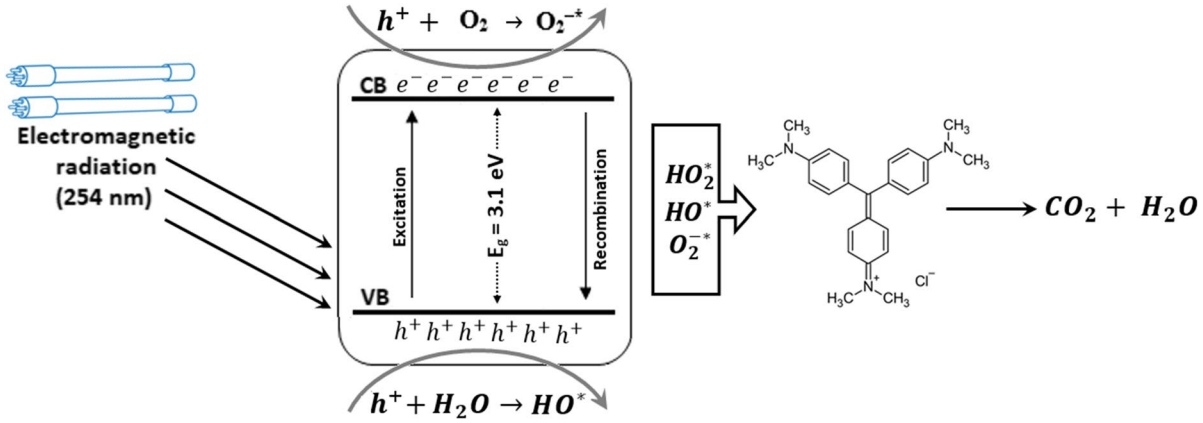

Fig. 9 Schematic illustration of the photodegradation mechanism of CV in the presence of $CoCuFe_2O_4$

Table 3 Degradation kinetics of CV in the presence of $CoCuFe_2O_4$ nanoparticles

Kinetic model	Mathematical expression	Rate constant	R^2
Zero order	$C = -kt + C_o$	$4.0E^{-9}$ mol.L^{-1}.min^{-1}	0.9932
First order	$ln\left(\frac{C_o}{C}\right) = k_1 t$	$2.3E^{-3}$ min^{-1}	0.9894
Second order	$\frac{1}{C} = \frac{1}{C_o} + k_2 t$	$2.0E^{-2}$ L.mol^{-1}.min^{-1}	0.9538

nanoparticle-induced erythrocyte cell disruptions and making reasonable corrections for different cell types. In this study, hemolytic activity tests were performed to examine the effects of $CoCuFe_2O_4$ NPs on RBCs. In Fig. 10a and b, aggregation of cell membranes of completely lysed erythrocytes incubated in pure water (due to high osmolarity) and healthy normal erythrocyte cells having a highly specific biconcave shape and a pallor area in the center is shown, respectively. Oxidative stress-induced erythrocyte deformations generated by $CoCuFe_2O_4$ NPs with 1.0 mg mL^{-1} and 5.0 mg mL^{-1} are shown in Fig. 10c and d, respectively. While lots of healthy normal RBCs are counted in 1.0 mg mL^{-1} treatment, RBCs treated with 5.0 mg mL^{-1} $CoCuFe_2O_4$ have different types of deformations (schistocytes, spherocytes, Heinz bodies). Heinz bodies and an increased degree of variation in cell morphology (poikilocytosis) [57] was clearly visible in Fig. 10d. When cells are exposed to oxidative stress, ROS start attacking the bonds between heme unit and globin moieties in the hemoglobin molecule. Globin units leave from the hemoglobin complex, form little aggregates, and stick to the inside of the RBC membrane. These inclusions composed of oxidized denatured hemoglobin are called Heinz bodies [58] (Fig. 10d). Heinz bodies form mainly during intense oxidative stress and hemolysis occurs after appearing inclusions in the erythrocytes [59]. In 1.0 mg mL^{-1} $CoCuFe_2O_4$ application, a fragmented RBC (schistocyte) was observed as evidence for erythrocyte lysis; nevertheless, the degree of hemolysis was below the acceptable level of 5%. On the contrary, at 1.0 mg mL^{-1} $CoCuFe_2O_4$ application (Fig. 10d), lots of deformed cells (poikilocytosis) including Heinz bodies and spherocytes were detected. Spherocytes which are observed in all hemolytic anemias are considered as evidence of extravascular factor-mediated hemolysis that forces the blood cell to have spherical shape [28, 60, 61].

As shown in Fig. 11, the supernatant of the 1.0 mg mL^{-1} $CoCuFe_2O_4$ application was colorless and transparent, demonstrating the negligible hemolysis ratio. However, at 5.0 mg mL^{-1} $CoCuFe_2O_4$ application, supernatant phase showed a bright red color, indicating the presence of an obvious hemolysis phenomena. While the AHR for human erythrocytes subjected to 5.0 mg mL^{-1} $CoCuFe_2O_4$ concentration was 12.4%, it was only 2.2% for those of exposed to 1.0 mg mL^{-1} $CoCuFe_2O_4$ which was lower than the allowed limit that is 5% [51, 62].

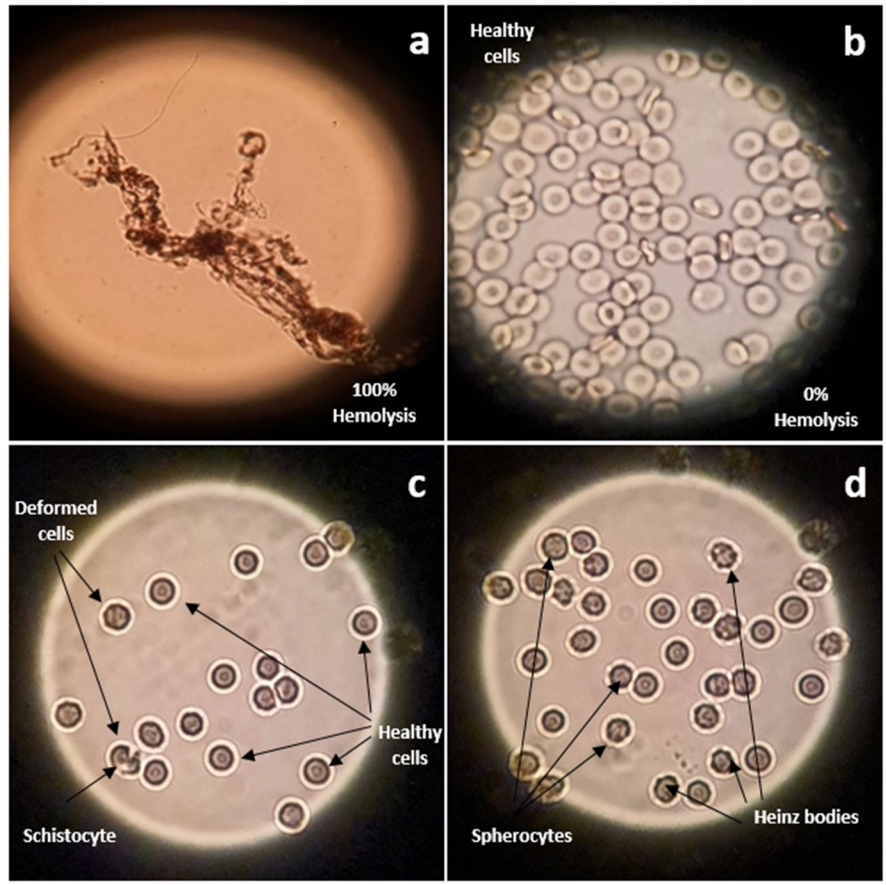

Fig. 10 Optical microscope images of RBCs (80 × magnification) in **a** positive control, **b** negative control, **c** 1.0 mg mL^{-1} $CoCuFe_2O_4$ and **d** 5.0 mg $mL.^{-1}$ $CoCuFe_2O_4$

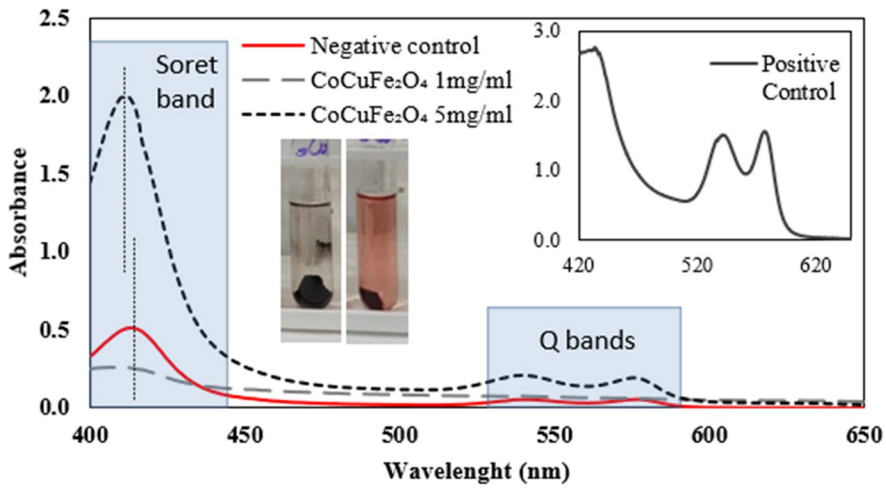

Fig. 11 UV–Vis spectra of erythrocyte suspensions treated with PBS alone (negative control) and $CoCuFe_2O_4$ nanoparticles with 1.0 mg mL^{-1} and 5.0 mg mL^{-1} concentrations (after incubation and centrifugation). Insets: UV–Vis spectra of erythrocyte suspension in positive control test and after centrifugation digital photos of $CoCuFe_2O_4$ samples in 1.0 mg mL^{-1} (left) and 5.0 mg mL^{-1} (right) concentrations

The porphyrin ring system consists of four highly conjugated pyrrole rings linked by methane bridges. The heme moiety in Hb is the Fe(II) complex of protoporphyrin ($Hb\left(Fe^{2+}\right)$), which carries a methyl group and a vinyl or propionic acid unit in each pyrrole ring. ROS produced on the surface of $CoCuFe_2O_4$ NPs would be responsible from the oxidation of hem iron into Fe(III) and the formation of methemoglobin (MHb). In MHb having the ferric state iron, the oxygen binding capacity

of the molecule is significantly reduced. MHb ($(Hb(Fe^{3+})OH$) in Eq. 18 can also be formed in a small amount under the influence of various substances such as heavy metal ions or phenolics that are exposed in daily life [63, 64]. In a healthy metabolic process, it is reduced by intracellular enzymatic reactions and converted back to Hb having a Fe^{2+} carrying ferroprotoporphyrin system [65]. MHb reduction systems, in which NADH cytochrome b5 reductase and glutathione are primarily effective (Eq. 19–20), prevent MHb from exceeding 1% of the total Hb concentration [66]. Glutathione is an antioxidant which protects cells from the toxic effects of oxidants such as free radicals, peroxides, and heavy metals. Glutathione is found in erythrocytes and protects the cell from oxidative stress with the effect of enzymes such as superoxide dismutase and glutathione peroxidase [67]:

$$Hb(Fe^{2+}) + ROS \rightarrow Hb(Fe^{3+})OH \quad (18)$$

$$Hb(Fe^{3+})\ OH \xrightarrow{Glutathione} Hb(Fe^{2+}) \quad (19)$$

$$Hb(Fe^{3+})OH \xrightarrow{NADH\,cytochrome\,b_5\,reductase} Hb(Fe^{2+}) \quad (20)$$

Another possible $CoCuFe_2O_4$–blood interaction may be the interaction of Co–Cu and Fe^{2+} in protoporphyrin ring system. Selective separation of some specific molecules is difficult due to interferences created by protein-based molecules which are abundant in blood. Chelating species such as Cu and Co in the structure of nano-sized materials make them suitable for being used in selective separation. Cu^{2+}, Co^{2+}, Ni^{2+}, or Fe^{2+} containing NPs form covalent interactions and chelates especially with histidine-rich proteins. In a related literature study conducted by Thomas et al. [68], it was emphasized that ferrite-based NPs can be used in the chemical recognition of some molecules and in the selective separation and fractionation of blood proteins. In the study of Guo et al. [69], sol–gel-synthesized $CuFe_2O_4$ NPs were investigated for their chelating properties and photoactivities towards methylene blue. In another study, solvothermally synthesized $CuFe_2O_4$ particles were investigated for their performances to be used in the selective separation of hemoglobin- and histidine-bearing proteins [70]. Superparamagnetic $CoFe_2O_4$ NPs synthesized by seed-mediated growth method were also investigated for selective separation, enrichment, and characterization of phosphoproteins [71].

In this study, although the $CoCuFe_2O_4$ NPs seem to have good biocompatibility especially at 1.0 mg mL^{-1} concentration just by considering the hemolysis rates, when the full spectrum is examined, changes indicative of the potential interactions of the samples with blood components are striking. One of the most probable interactions of $CoCuFe_2O_4$ NPs and blood components is the oxidation of hem units as a direct result of ROS production by NPs. The decrease in intensity in the Q band at 1.0 mg mL^{-1} nanoparticle concentration is an indicator showing the presence of Fe^{3+} in the ferroprotoporphyrin system and proving the formation of MHb. At the same time, the characteristic change in the oxyhemoglobin Q bands is found as another evidence confirming MHb formation [72]. The UV spectrum of 1.0 mg mL^{-1} $CoCuFe_2O_4$ nanoparticle concentration also shows a significant blue shift and decrease in intensity in the Soret band, which are indicative of the oxidation of Hb to MHb because of oxidative stress created by ROS in erythrocytes (Fig. 11).

At 5.0 mg mL^{-1} $CoCuFe_2O_4$ NP concentration, the main and dominant interaction is between NPs and the erythrocyte cell wall. Erythrocyte membrane is a composite structure, primarily composed of a phospholipid bilayer bearing almost the same concentrations of both lipid and protein moieties [73, 74]. NPs inactivate proteins in the erythrocyte membrane, causing cell death. NPs form R–S–$(Cu)^{2+}$–S–R complexes by interacting with proteins in the membrane structure, especially those carrying sulfhydryl (-SH) groups such as cysteine. These interactions reduce erythrocyte membrane permeability and ultimately result in lysis of the erythrocyte cell wall [75, 76]. In Fig. 11, along with the characteristic red color of hemoglobin leaking out of the cell as a result of lysis of the erythrocyte cell wall, a small amount of blue shift in the Soret band was also observed as an indicator of MHb formation. One of the main reasons for the deterioration of erythrocyte cell integrity is the destruction of the erythrocyte membrane by ROS such as superoxide and hydroxyl radicals. Thus, hemolysis at 5.0 mg mL^{-1} $CoCuFe_2O_4$ nanoparticle concentration can be attributed to the

comparatively high amount of ROS formed by $CoCuFe_2O_4$ NPs, which is also consistent with the results of photodegradation experiments.

Conclusion

$CoCuFe_2O_4$ spinel ferrites were synthesized by the co-precipitation method using $Fe(NO_3)_3.9H_2O$, $Co(NO_3)_2.6H_2O$, and $Cu(NO_3)_2.3H_2O$. NPs have a high crystalline quality; no secondary crystalline phases in addition to the cubic structured spinel lattice were observed and exhibited an agglomerated structure. SEM images showed the agglomerated morphology of $CoCuFe_2O_4$ NPs. UV–Vis diffuse reflectance spectra was interpreted, and direct and indirect band gap energies were determined as 1.93 eV and 0.6 eV, respectively. Photocatalytic properties of $CoCuFe_2O_4$ NPs were attributed to the formation of ROS such as HO^* and O_2^{-*} triggered by the photo-excitation of electrons from valence band to conduction band. The decomposition of CV under the influence of ROS formed on the nanoparticle surface was determined as 64.9%. Three different kinetic models were tested to explain the CV photodegradation kinetics. Among them, it was concluded that the zero-order kinetics ($R^2 = 0.9932$) was the best fitted model for the CV photodegradation reaction. Blood compatibility tests showed that $CoCuFe_2O_4$ did not cause hemolysis at 1 mg mL^{-1} concentration; however, a blue shift in the Soret band with a decrease in intensity and the disappearance of the Q bands demonstrated the formation of MHb. It was concluded that erythrocyte lysis at 5.0 mg mL^{-1} concentration was caused by high amount of ROS produced by NPs, which also caused oxidation of heme units on the porphyrin ring. Microscopic images of erythrocytes showed spherocytes, schistocytes, and Heinz bodies at a concentration of 5.0 mg mL^{-1} NPs, while large number of healthy cells was detected at 1.0 mg mL^{-1}. Photocatalytic activity test results and RBC deformations were evaluated together, and it was concluded that NPs showed cytotoxic effects, especially at high concentrations, associated with ROS. It is hoped that the findings from this study will be developed with subsequent research and modifications, thus leading to the development of nanomaterials with better biocompatibility and adapted structural properties.

Data availability The author confirms that the data supporting the findings of this study are available within the article.

Declarations

Competing interests The author declares no competing interests.

References

1. Rajan A, Sharma M, Sahu NK (2020) Assessing magnetic and inductive thermal properties of various surfactants functionalised Fe_3O_4 nanoparticles for hyperthermia. Sci Report 10:1–15. https://doi.org/10.1038/s41598-020-71703-6
2. Yang X, Zheng G, Wang Q, Chen X, Han Y, Zhang D, Zhang Y (2022) Functional application of multi-element metal composite materials. J Alloys Compd 895:162622
3. Joshi R, Singh BP, Ningthoujam RS (2020) Confirmation of highly stable 10 nm sized Fe_3O_4 nanoparticle formation at room temperature and understanding of heat-generation under AC magnetic fields for potential application in hyperthermia. AIP Adv 10:105033. https://doi.org/10.1063/5.0022446
4. Mousavi SM, Hashemi SA, Zarei M, Bahrani S, Savardashtaki A, Esmaeili H, Ramavandi B (2020) Data on cytotoxic and antibacterial activity of synthesized Fe_3O_4 nanoparticles using Malva sylvestris. Data Br 28:104929. https://doi.org/10.1016/j.dib.2019.104929
5. Pachaiappan R, Manavalan K (2021) Role of metals, metal oxides, and metal sulfides in the diagnosis and treatment of cancer. In: Rajendran S, Naushad M, Durgalakshmi D, Lichtfouse E (eds) Metal, Metal Oxides and Metal Sulphides for Biomedical Applications. Environmental Chemistry for a Sustainable World, vol 58. Springer, Cham
6. Gholami A, Mousavi SM, Hashemi SA, Ghasemi Y, Chiang WH, Parvin N (2020) Current trends in chemical modifications of magnetic nanoparticles for targeted drug delivery in cancer chemotherapy. Drug Metab Rev 52:205–224. https://doi.org/10.1080/03602532.2020.1726943
7. Gaikwad P, Sabale S, Kurane R, Kakade B, Parase H, Dhabbe R, Kamble P (2021) Magneto-structural properties and reliability of (Mn/Ni/Zn) substituted cobalt-copper ferrite heterogeneous catalyst for selective and efficient oxidation of aryl alcohols. Inorg Nano-Met 1–14. https://doi.org/10.1080/24701556.2021.1980036
8. Yalcin B, Ozcelik S, Icin K, Senturk K, Ozcelik B, Arda L (2021) Structural, optical, magnetic, photocatalytic activity and related biological effects of $CoFe_2O_4$ ferrite nanoparticles. J Mater Sci Mater 32:13068–13080. https://doi.org/10.1007/s10854-021-05752-6
9. Ozcelik S, Yalçın B, Arda L, Santos H, Sáez-Puche R, Angurel LA, Ozcelik B (2021) Structure, magnetic, photocatalytic and blood compatibility studies of nickel nanoferrites prepared by laser ablation technique in distilled water. J Alloys Compd 854:157279. https://doi.org/10.1016/j.jallcom.2020.157279

10. Senol SD, Yalcin B, Ozugurlu E, Arda L (2020) Structure, microstructure, optical and photocatalytic properties of Mn-doped ZnO nanoparticles. Mater Res Express 7:015079. https://doi.org/10.1088/2053-1591/ab5eea
11. Heiba ZK, Mohamed MB, Arda L, Dogan N (2015) Cation distribution correlated with magnetic properties of nanocrystalline gadolinium substituted nickel ferrite. J Magn Magn Mater 391:195–202. https://doi.org/10.1016/j.jmmm.2015.05.003
12. Nikazar S, Barani M, Rahdar A, Zoghi M, Kyzas GZ (2020) Photo-and magnetothermally responsive nanomaterials for therapy, controlled drug delivery and imaging applications. Chem Select 5:12590–12609. https://doi.org/10.1002/slct.202002978
13. Kossatz S, Grandke J, Couleaud P, Latorre A, Aires A, Crosbie-Staunton K, Calero M (2015) Efficient treatment of breast cancer xenografts with multifunctionalized iron oxide nanoparticles combining magnetic hyperthermia and anti-cancer drug delivery. Breast Cancer Res 17:66. https://doi.org/10.1186/s13058-015-0576-1
14. Junaid M, Qazafi IA, Khan MA, Gulbadan S, Ilyas SZ, Somaily HH, Amin MA (2022) The influence of Zr and Ni co-substitution on structural, dielectric and magnetic traits of lithium spinel ferrites. Ceram Int 48(10):14307–14314. https://doi.org/10.1016/j.ceramint.2022.01.320
15. Jacinto MJ, Ferreira LF, Silva VC (2020) Magnetic materials for photocatalytic applications - a review. J Solgel Sci Technol 96:1–14. https://doi.org/10.1007/s10971-020-05333-9
16. Bahrami M, Derikvand Z (2022) Fabrication of a new magnetic $CoFe_2O_4$/ZrMCM-41 nanocomposite: simple construction and application for fast reduction of Cr (IV) and nitroaromatic compounds. J Molec Str 1254:132367. https://doi.org/10.1016/j.molstruc.2022.132367
17. Zhang J, Liu P, Ren Y, Du Y, Geng C, Ma J, Zhao F (2022) Treatment of shale gas produced water by magnetic $CuFe_2O_4$/TNTs hybrid heterogeneous catalyzed ozone: efficiency and mechanisms. J Hazard Mater 423:127124
18. Amiri M, Salvati-Niasari M, Akbari A (2019) Magnetic nanocarriers: evolution of spinel ferrites for medical applications. Adv Colloid Interface Sci 265:29–44. https://doi.org/10.1016/j.cis.2019.01.003
19. Oh Y, Moorthy MS, Manivasagan P, Bharathiraja S, Oh J (2017) Magnetic hyperthermia and pH-responsive effective drug delivery to the sub-cellular level of human breast cancer cells by modified $CoFe_2O_4$ nanoparticles. Biochimie 133:7–19. https://doi.org/10.1016/j.biochi.2016.11.012
20. Chapman MC, Lee AY, Hayward JH, Joe BN, Price ER (2020) Superparamagnetic iron oxide sentinel node tracer injection: effects on breast MRI quality. J Breast Imaging 2:577–582. https://doi.org/10.1093/jbi/wbaa083
21. Ansari SM, Bhor RD, Pai KR, Mazumder S, Sen D, Kolekar YD, Ramana CV (2016) Size and chemistry controlled cobalt-ferrite nanoparticles and their anti-proliferative effect against the MCF-7 breast cancer cells. ACS Biomater Sci Eng 2:2139–2152. https://doi.org/10.1021/acsbiomaterials.6b00333
22. Zarrabi M, Afzal E, Ebrahimi M (2018) Manipulation of hematopoietic stem cell fate by small molecule compounds. Stem Cells Dev 27:1175–1190. https://doi.org/10.1089/scd.2018.0091
23. Sunitha Y, Kumar S (2021) An assessment of vitamin B12 through determination of cobalt by X-ray fluorescence spectrometry. Radiat Phys Chem 188:109583. https://doi.org/10.1016/j.radphyschem.2021.10958
24. Sattarahmady N, Zare T, Mehdizadeh AR, Azarpira N, Heidari M, Lotfi M, Heli H (2015) Dextrin-coated zinc substituted cobalt-ferrite nanoparticles as an MRI contrast agent: in vitro and in vivo imaging studies. Colloids Surf B 129:15–20. https://doi.org/10.1016/j.colsurfb.2015.03.021
25. Wahler T, Schuster R, Libuda J (2020) Self-metalation of anchored porphyrins on atomically defined cobalt oxide surfaces: in situ studies by surface vibrational spectroscopy. Chemistry 26:12445. https://doi.org/10.1002/chem.202001331
26. Yao M, Ma M, Zhang H, Zhang Y, Wan G, Shen J, Wu R (2018) Mesopore-induced aggregation of cobalt protoporphyrin for photoacoustic imaging and antioxidant protection of stem cells. Adv Funct Mater 28:1804497. https://doi.org/10.1002/adfm.201804497
27. Liu T, Xiao B, Xiang F, Tan J, Chen Z, Zhang X, Deng J (2020) Ultrasmall copper-based nanoparticles for reactive oxygen species scavenging and alleviation of inflammation related diseases. Nat Commun 11:1–16. https://doi.org/10.1038/s41467-020-16544-7
28. Agarwal V, Gupta V, Bhardwaj VK, Singh K, Khullar P, Bakshi M (2022) Hemolytic response of iron oxide magnetic nanoparticles at the interface and in bulk: extraction of blood cells by magnetic nanoparticles. ACS Appl Mater Interfaces 14:6428–6441
29. Yadav S, Maurya PK (2022) Recent advances in the protective role of metallic nanoparticles in red blood cells. Biotech 12:1–13
30. Bai C, Hu P, Liu N, Feng G, Liu D, Chen Y, Zhang Y (2020) Synthesis of ultrasmall Fe_3O_4 nanoparticles as T 1–T 2 dual-modal magnetic resonance imaging contrast agents in rabbit hepatic tumors. ACS Appl Nano Mater 3:3585–3595. https://doi.org/10.1021/acsanm.0c00306
31. Vangijzegem T, Stanicki D, Panepinto A, Socoliuc V, Vekas L, Muller RN, Laurent S (2020) Influence of experimental parameters of a continuous flow process on the properties of very small iron oxide nanoparticles (VSION) designed for T1-weighted magnetic resonance imaging (MRI). Nanomaterials 10:757. https://doi.org/10.3390/nano10040757
32. Du H, Akakuru OU, Yao C, Yang F, Wu A (2022) Transition metal ion-doped ferrites nanoparticles for bioimaging and cancer therapy. Transl Oncol 15:101264
33. Kumari S, Manglam MK, Kumar L, Seal P, Borah JP, Kumar Zope M, Kar M (2022) Magnetic properties and hyperthermia action of cobalt zinc ferrite fibers. J Sol-Gel Sci Technol 101:546–561. https://doi.org/10.1007/s10971-022-05737-9
34. Sharma VK, Bielski BH (1991) Reactivity of ferrate (VI) and ferrate (V) with amino acids. Inorg Chem 30:4306–4310. https://doi.org/10.1021/ic00023a005
35. Xiong Z, Lai B, Yang P, Zhou Y, Wang J, Fang S (2015) Comparative study on the reactivity of Fe/Cu bimetallic particles and zero valent iron (ZVI) under different conditions of N_2, air or without aeration. J Hazard Mater 297:261–268. https://doi.org/10.1016/j.jhazmat.2015.05.006

36. Jiang K, Zhang L, Bao G (2021) Magnetic iron oxide nanoparticles for biomedical applications. Curr Opin Biomed Eng 20:100330. https://doi.org/10.1016/j.cobme.2021.100330
37. Kumar G, Katoch G (2021) Recent advances in processing, characterizations and biomedical applications of spinel ferrite nanoparticles. Materials Research Foundations 112:62–120. https://doi.org/10.21741/9781644901595-2
38. Nosheen S, Irfan M, Abidi SH, Syed Q, Habib F, Asghar A, Waseem B, Soomro B, Butt H, Akram M (2021) A review: development of magnetic nan o vectors for biomedical applications. GSC Adv Res Rev 8:85–110. https://doi.org/10.30574/gscarr.2021.8.2.0169
39. Matloubi Moghaddam F, Pourkaveh R, Ahangarpour M (2018) Cobalt-copper ferrite nanoparticles catalyzed click reaction at room-temperature: green access to 1, 2, 3-triazole derivatives. Chem Select 3:2586–2593. https://doi.org/10.1002/slct.201800134
40. Dave PN, Sirach R, Deshpande MP (2022) Evaluating the effect of nanosized $CoCuFe_2O_4$ for thermal decomposition of nitrotriazolone high energetic material. Chem Select 7:e202202071. https://doi.org/10.1002/slct.202202071
41. Yalcin B, Erbil C (2018) Effect of sodium hydroxide solution as polymerization solvent and activator on structural, mechanical and antibacterial properties of PNIPAAm and P (NIPAAm–clay) hydrogels. Polym Compos 39:E386–E406. https://doi.org/10.1002/pc.24490
42. Dadaei M, Naeimi H (2020) An environment-friendly method for green synthesis of pyranopyrazole derivatives catalyzed by $CoCuFe_2O_4$ magnetic nanocrystals under solvent-free conditions. Polycycl Aromat Compd 42:204–217. https://doi.org/10.1080/10406638.2020.1725897
43. Moghaddam FM, Pourkaveh R, Ahangarpour M (2017) Nano $CoCuFe_2O_4$ catalyzed coupling reaction of acid chlorides with terminal alkynes: a powerful toolbox for palladium-free ynone synthesis. Catal Commun 102:71–75. https://doi.org/10.1016/j.catcom.2017.08.029
44. Jamil H, Dildar IM, Ilyas U, Hashmi JZ, Shaukat S, Sarwar MN, Khaleeq-ur-Rahman M (2021) Microstructural and optical study of polycrystalline manganese oxide films using Kubelka-Munk function. Thin Solid Films 732:138796. https://doi.org/10.1016/j.tsf.2021.138796
45. Chavan P, Naik LR (2017) Investigation of energy band gap and conduction mechanism of magnesium substituted nickel ferrite nanoparticles. Phys Status Solidi 214:1700077. https://doi.org/10.1002/pssa.201700077
46. Khan HAA, Ullah S, Rehman G, Khan S, Ahmad I (2021) First principle study of band gap nature, spontaneous polarization, hyperfine field and electric field gradient of desirable multiferroic bismuth ferrite ($BiFeO_3$). J Phys Chem Solids 148:109737. https://doi.org/10.1016/j.jpcs.2020.109737
47. Siva KV, Kumar A, Chelvane JA, Arockiarajan A (2022) Structural, magnetic, magnetostrictive and optical properties of Mn and Cu codoped cobalt ferrite. Mater Sci Eng, B 284:115885. https://doi.org/10.1016/j.mseb.2022.115885
48. Hammad TM, Kuhn S, Amsha AA, Hempelmann R (2021) Investigation of structural, optical, and magnetic properties of Co2+ ions substituted CuFe2O4 spinel ferrite nanoparticles prepared via precipitation approach. J Aust Ceram Soc 57:543–553. https://doi.org/10.1007/s41779-020-00556-z
49. Mirzaee S, Mahdavifar S, Shayesteh SF (2018) Experimental and theoretical investigations of magnetic properties of Co ferrite/polyvinyl alcohol nanocomposites. J Supercond Nov Magn 31:217–223. https://doi.org/10.1007/s10948-017-4166-6
50. Yalcin B, Akcan D, Yalcin IE, Alphan MC, Senturk., Ozyigit II, Arda L, (2020) Effect of Mg doping on morphology, photocatalytic activity and related biological properties of $Zn_{1-x}Mg_xO$ nanoparticles. Turk J Chem 44:1177–1199. https://doi.org/10.3906/kim-2004-9
51. Bhaskar N, Sulyaeva V, Gatapova E, Kaichev V, Khomyakov M, Kolodin A, Basu B (2022) On the origin of better hemocompatibility of the $BC_xN_yO_z$ coatings. Appl Surf Sci 576:151760. https://doi.org/10.1016/j.apsusc.2021.151760
52. Frolova LA, Khmelenko OV (2020) The study of Co–Ni-Mn ferrites for the catalytic decomposition of 4-nitrophenol. Catal Lett 151:1522–1533. https://doi.org/10.1007/s10562-020-03419-1
53. Rani M, Shanker U, Chaurasia AK (2017) Catalytic potential of laccase immobilized on transition metal oxides nanomaterials: degradation of alizarin red S dye. J Environ Chem Eng 5:2730–2739. https://doi.org/10.1016/j.jece.2017.05.026
54. Oladoja NA, Anthony ET, Ololade IA, Saliu TD, Bello GA (2018) Self-propagation combustion method for the synthesis of solar active Nano Ferrite for Cr (VI) reduction in aqua system. J Photochem Photobiol 353:229–239. https://doi.org/10.1016/j.jphotochem.2017.11.026
55. Pleskova SN, Gornostaeva EE, Kryukov RN, Boryakov AV, Zubkov SY (2018) Changes in the architectonics and morphometric characteristics of erythocytes under the influence of magnetite nanoparticles. Cell Tissue Biol 12:127–134. https://doi.org/10.1134/S1990519X18020086
56. Zemlyanova MA, Zaitseva NV, Ignatova AM, Stepankov MS, Toropov LI, Kol'dibekova YV, (2021) Study of hematological parameters and morphometric indices of erythrocytes in rats exposed to calcium oxide nanoparticles. Bull Exp Biol Med 170:665–668. https://doi.org/10.1007/s10517-021-05128-0
57. Corrons JLV, Bain BJ (2022) Haemoglobin Bristol-Alesha in a child with non-spherocytic severe haemolytic anaemia and marked anisochromic poikilocytosis with basophilic stippling and amorphous intracellular content. Blood Cells Mol Dis 94:102652. https://doi.org/10.1016/j.bcmd.2022.102652
58. Thiagarajan P, Parker CJ, Prchal JT (2021) How do red blood cells die? Front Physiol 12:318
59. Mameri A, Bournine L, Mouni L, Bensalem S, Iguer-Ouada M (2021) Oxidative stress as an underlying mechanism of anticancer drugs cytotoxicity on human red blood cells' membrane. Toxicol in Vitro 72:105106. https://doi.org/10.1016/j.tiv.2021.105106
60. Johnson S (2021) Review on spherocytosis. J Hematol Thrombo Dis 9:445
61. Agarwal V, Gupta V, Bhardwaj VK, Singh K, Khullar P, Bakshi MS (2021) Avoiding hemolytic anemia by understanding the effect of the molecular architecture of Gemini surfactants on hemolysis. Langmuir 37:3709–3720. https://doi.org/10.1021/acs.langmuir.1c00154
62. Singh S, Singh G, Bala N (2021) Synthesis and characterization of iron oxide-hydroxyapatite-chitosan composite coating and its biological assessment for biomedical

applications. Prog Org Coat 150:106011. https://doi.org/10.1016/j.porgcoat.2020.106011
63. Iolascon A, Bianchi P, Andolfo I, Russo R, Barcellini W, Fermo E (2021) SWG of red cell and iron of EHA and EuroBloodNet, Recommendations for diagnosis and treatment of methemoglobinemia. Am J Hematol 96:1666–1678. https://doi.org/10.1002/ajh.26340
64. Arnhold J (2019) Cell and tissue destruction: mechanisms, protection, disorders. Academic Press
65. Cortazzo JA, Lichtman AD (2014) Methemoglobinemia: a review and recommendations for management. J Cardiothorac Vasc Anesth 28:1043–1047. https://doi.org/10.1053/j.jvca.2013.02.005
66. Keohane E, Otto CN, Walenga J (2019) Rodak's Hematology-E-Book: Clinical Principles and Applications. Elsevier Health Sciences
67. Chu L, Wu Y, Xu X, Phillips L, Kolodrubetz D (2020) Glutathione catabolism by Treponema denticola impacts its pathogenic potential. Anaerobe 62:102170. https://doi.org/10.1016/j.anaerobe.2020.102170
68. Thomas SL, Thacker JB, Schug KA, Maráková K (2021) Sample preparation and fractionation techniques for intact proteins for mass spectrometric analysis. J Sep Sci 44:211–246. https://doi.org/10.1002/jssc.202000936
69. Guo X, Wang K, Xu Y (2019) Tartaric acid enhanced $CuFe_2O_4$-catalyzed heterogeneous photo-Fenton-like degradation of methylene blue. Mater Sci Eng B 245:75–84. https://doi.org/10.1016/j.mseb.2019.05.015
70. Zheng J, Lin Z, Liu W, Wang L, Zhao S, Yang H, Zhang L (2014) One-pot synthesis of $CuFe_2O_4$ magnetic nanocrystal clusters for highly specific separation of histidine-rich proteins. J Mater Chem B 2:6207–6214. https://doi.org/10.1039/C4TB00986J
71. Chen B, Hwang L, Ochowicz W, Lin Z, Guardado-Alvarez TM, Cai W, Ge Y (2017) Coupling functionalized cobalt ferrite nanoparticle enrichment with online LC/MS/MS for top-down phosphoproteomics. Chem Sci 8:4306–4311. https://doi.org/10.1039/C6SC05435H
72. Denzer ML, Mowery C, Comstock HA, Maheswarappa NB, Mafi G, VanOverebeke DL, Ramanathan R (2020) Characterization of the cofactors involved in non-enzymatic metmyoglobin/methemoglobin reduction. In Vitro Meat Muscle Biol 4:1–10. https://doi.org/10.22175/mmb.9507
73. Cho Y, Woo JH, Kwon OS, Yoon SS, Son J (2019) Alterations in phospholipid profiles of erythrocytes deep-frozen without cryoprotectants. Drug Test Anal 11:1231–1237. https://doi.org/10.1002/dta.2600
74. Sathi A, Viswanad V, Aneesh TP, Kumar BA (2014) Pros and cons of phospholipid asymmetry in erythrocytes. J Pharm Bioallied Sci 6:81. https://doi.org/10.4103/0975-7406.129171
75. Tkachenko A, Onishchenko A, Klochkov V, Kavok N, Nakonechna O, Yefimova S, Posokhov Y (2020) The impact of orally administered gadolinium orthovanadate $GdVO_4$: Eu^{3+} nanoparticles on the state of phospholipid bilayer of erythrocytes. Turkish J Biochem 45:389–395. https://doi.org/10.1515/tjb-2019-0427
76. Azzam EMS, Zaki MF (2016) Surface and antibacterial activity of synthesized nonionic surfactant assembled on metal nanoparticles. Egypt J Pet 25:153–159. https://doi.org/10.1016/j.ejpe.2015.04.005